Numerical analysis of heat transfer enhancement on steam condensation in the presence of air outside the tube

Wen-Tao Li[1] · Xian-Ke Meng[2] · Hao-Zhi Bian[1] · Ming Ding[1]

Abstract In loss-of-coolant accidents, a passive containment heat removal system protects the integrity of the containment by condensing steam. As a large amount of air exists in the containment, the steam condensation heat transfer can be significantly reduced. Based on previous research, traditional methods for enhancing pure steam condensation may not be applicable to steam–air condensation. In the present study, new methods of enhancing condensation heat transfer were adopted and several potentially enhanced heat transfer tubes, including corrugated tubes, spiral fin tubes, and ring fin tubes were designed. STAR-CCM+ was used to determine the effect of enhanced heat transfer tubes on the steam condensation heat transfer. According to the calculations, the gas pressure ranged from 0.2 to 1.6 MPa, and air mass fraction ranged from 0.1 to 0.9. The effective perturbation of the high-concentration air layer was identified as the key factor for enhancing steam–air condensation heat transfer. Further, the designed corrugated tube performed well at atmospheric pressure, with a maximum enhancement of 27.4%, and performed poorly at high pressures. In the design of spiral fin tubes, special attention should be paid to the locations that may accumulate high-concentration air. Nonetheless, the ring-fin tubes generally displayed good performance under all conditions of interest, with a maximum enhancement of 24.2%.

✉ Hao-Zhi Bian
   bianhaozhi@hrbeu.edu.cn

✉ Ming Ding
   dingming@hrbeu.edu.cn

1   Heilongjiang Provincial Key Laboratory of Nuclear Power System and Equipment, Harbin Engineering University, Harbin 150001, China

2   China Nuclear Engineering Consulting Co., Ltd., Beijing 100073, China

1 Introduction

In the scenarios of a main steam line break accident or loss of coolant accident, a large amount of high-temperature steam is discharged into the atmospheric space in the containment. If the accidents are coupled with a station blackout, some active safety measure facilities may fail, and the temperature and pressure in the reactor containment will continue to increase. When the pressure exceeds the design limit, the reactor containment may be destroyed, and radioactive material will be released into the environment. This release can be harmful to the public and the environment, and may result in serious consequences. To prevent this type of accident, third-generation advanced nuclear power units are currently equipped with a passive containment heat removal system (PCS) [1, 2]. The PCS condenses steam inside the containment without external power [3] and can remove heat from the containment through density differences, etc.

The first containment was built with steel at the Knowles nuclear power laboratory in the USA. Nowadays, some third-generation advanced nuclear power plants, such as AP1000, still use steel containment. Notably, the heat inside the steel containment can be removed via spraying

with water. The steel containment is expensive. In contrast, many third-generation advanced nuclear power systems, such as HPR1000, use concrete containment, where heat cannot be removed via spraying with water. Thus, this reactor must have a PCS heat exchanger in the containment to remove heat and the containment pressure must be maintained within the safety threshold. Considering the harsh environment in the containment gas space, compact heat transfer with higher efficiency is required for the further development of passive safety technology [4]. Therefore, the heat transfer enhancement of the PCS heat exchangers must be evaluated.

A large amount of steam enters the containment when a loss-of-coolant accident (LOCA) occurs [5]. The PCS heat exchanger exports heat by condensing steam and the air in the containment reduces the effect of condensing steam in the PCS heat exchanger. To achieve an optimal design of PCS heat transfer, heat transfer enhancement studies on steam condensation consisting of air are necessary.

Several assessments on pure steam condensation have been conducted. The pure steam condensation can have a stronger consolidated heat transfer capability than film condensation by thinning the liquid film on the heat transfer surface or via dropwise condensation [6, 7]. However, steam condensation with air is quite different from pure steam condensation [8]. When steam condensation in the presence of air, a highly concentrated air layer is formed near the heat transfer tube, and the steam must pass through the air layer before condensation. The high-concentration air layer close to the heat transfer surface is the key factor influencing the condensation heat transfer behavior [9, 10]. Previously, when the mass fraction of air was 2%, the thermal resistance of the liquid film was only 5% of the total thermal resistance, and the temperature difference between the liquid film and wall surface was only 0.4 K [11]. Of note, the effect of the liquid film on heat transfer can be ignored. Therefore, a separate study on the enhancement of steam condensation using air is required.

Othmer [12] was the first to study this phenomenon experimentally, and many scholars have conducted subsequent research on this issue and obtained remarkable results.

To understand the general performance of steam–air condensation, many experimental studies have been conducted using flat panels and plain tubes [13, 14].

In 1965, Uchida [15] first proposed a correlation for the heat transfer coefficient for steam condensation in the presence of air, which only considers the air mass fraction. Subsequently, Bian [16], Su [17], Liu [18], Dehbi [19], and others combined their experimental data and fitted their experimental correlations. Accordingly, the new correlation fully considers the influence of related parameters,

such as the concentration of air, pressure, and wall sub-cooling.

In addition to experimental research, many researchers have conducted numerical simulations. At present, numerical simulations of condensation are based on three types of models: experimental models based on experimental correlations [20], mass diffusion models based on heat and mass transfer similarity theory [21], and theoretical models for solving control equations in the diffusion boundary layer and liquid film [22].

Heat-transfer enhancement is mainly divided into active and passive heat-transfer enhancements. Active heat transfer enhancement aims to enhance heat transfer by injecting pure steam near the heat transfer tube to blow away the non-condensable gas [23]. Notably, this method has a good heat-transfer enhancement effect. In fact, the heat transfer coefficient after steam injection was 1.18–1.77-fold higher than that without steam injection. This method requires an external power drive and is unsuitable for PCS systems. A passive heat transfer enhancement method is used to achieve bead condensation by adding organic coatings to the heat transfer tubes [24]. The heat transfer coefficient after bead condensation was 1.3–1.8-fold higher than that before bead condensation. Organic coatings are expensive, will easily fall off, and are unsuitable for PCS systems.

Changing the tube structure is a common method for enhancing the heat transfer. According to research on heat transfer enhancement tubes, structures such as corrugated tubes [25], vertically longitudinal finned tubes [26], and polished tubes had obvious enhancement in heat transfer under pure steam, and the enhancement of these structures could reach threefold that of a plain tube. However, when the steam contained air, the heat-transfer enhancement of the corrugated tube was only 10%. The longitudinally finned tube displayed heat transfer enhancement only when the air mass fraction was very large and showed inhibited heat transfer at an air mass fraction of less than 75%. The heat transfer coefficient was only 40% of that of the plain tube at an air mass fraction of 10%. The polishing tube [27] only affected the liquid film, with little or no disturbing effect on the air layer. Further, the liquid film had little effect on heat transfer. Thus, although the heat transfer coefficient increased compared with that of the plain tube, the enhancement was mainly within 10%.

In these studies, the proposed heat-transfer enhancement structures mainly performed well for pure steam condensation. However, the existing structure displayed poor enhancement when steam–air condensation occurred. Therefore, the local air concentration boundary layer distribution in the vicinity of the tube wall must be revealed and enhanced heat transfer structures must be designed according to the local heat and mass transfer behavior. In

this study, corrugated, ring fin, and spiral fin tubes were designed, and their effects on heat transfer were evaluated.

2 Calculation models

The CFD software, STAR-CCM+, was used to evaluate the heat-transfer enhancement of steam condensation in the presence of air outside the tube. The key aspect of the simulation involves the application of a proper condensation model to simulate the steam condensation process.

The condensation models commonly used in CFD simulations include experimental correlation and diffusion boundary layer models. The experimental correlation model was set according to the experiment, which was relatively simple. However, the applicability of this model is limited by the range of test parameters. Furthermore, this model is used to obtain the average heat transfer characteristics and pays less attention to the local heat transfer characteristics. As a result, measuring the diffusion and mass transfer of steam–air locally is a difficult task [28]. The diffusion boundary layer model forms a liquid film and an air layer at the surface and the mixed gas passes through the air layer to reach the interface between the liquid film and air layer for condensation. Accordingly, this model is suitable for simulating local phenomena [29]. In the simulation, a strengthened heat transfer structure combined with the local phenomenon was required [30]. Therefore, the diffusion boundary layer model served as a reasonable selection in this study.

2.1 Governing equations and turbulence model

In the simulation, the following control equations were used for the gas flow and heat transfer processes, except steam condensation.

Mass conservation:

$$\frac{\partial \rho}{\partial t} + \nabla(\rho w) = S_m \tag{1}$$

Momentum conservation:

$$\frac{\partial(\rho w)}{\partial t} + \nabla(\rho w w) = \nabla f_s + \rho f_v + S_{\rho v} \tag{2}$$

Energy conservation:

$$\frac{\partial(\rho E)}{\partial t} + \nabla(\rho w E) = \rho f_v w + \nabla(P w) + \nabla(k_{eff} \cdot \nabla T) + S_h \tag{3}$$

Species conservation:

$$\frac{\partial(\rho \omega_g)}{\partial t} + \nabla(\rho w \omega_g) = \nabla(\rho D_g \cdot \nabla \omega_g) + S_g \tag{4}$$

where ρ is the density, w is the velocity, S_m is the mass source term, $S_{\rho v}$ is the momentum source term, S_h is the energy source term, f_s is the surface force, f_v is the volume force, E is the energy, k_{eff} is the effective thermal conductivity, ω_g is the mass fraction of air, and D_g is the air diffusion coefficient.

An implicitly coupled solver is used in the calculation. Turbulence computing applications are used to obtain k-ε turbulence. As this model can provide good calculation results for phenomena, such as boundary layer separation and reflow, it can be selected in the simulation.

2.2 Steam condensation model

The condensing model was established according to the diffusion boundary layer model. The main thermal resistance during the condensation process occurred in the air layer, and a liquid film was formed on the tube surface. As the liquid film thickness is small, the thermal resistance of the liquid film is generally neglected [31]. Therefore, the effect of the liquid film was ignored in the model setup. The vapor condensation mass flux derived from the mass transfer equations of air and steam is expressed as:

$$m = \rho w \omega - \rho D \frac{\partial \omega}{\partial n}\bigg|_i \tag{5}$$

The condensation rate [32] derived from the mass transfer equations of air and steam is expressed as:

$$m_c = -\left(\frac{\rho D}{1 - \omega_v}\right) \cdot \left(\frac{\partial \omega_v}{\partial n}\right)\bigg|_i \tag{6}$$

The mixed gas diffusion coefficient D is usually calculated using the equation:

$$D = D_0 \left(\frac{T}{T_0}\right)^{1.75} \cdot \left(\frac{P_0}{P}\right) \tag{7}$$

If steam condensation occurs, the steam and the energy carried by the steam should be removed from the interface. The removal of vapors at the interface can be achieved by adding mass, momentum, and energy source terms to the first layer of the grid.

Mass source term:

$$S_m = -\left(\frac{\rho D}{1 - \omega_v}\right) \cdot \left(\frac{\partial \omega_v}{\partial n}\right)\bigg|_i \tag{8}$$

Momentum source term:

$$S_{\rho v} = S_m w \tag{9}$$

Energy source term:

$$S_h = S_m \overset{\bullet}{h} \tag{10}$$

where m is the mass flux, subscript c indicates condensation, ω is the mass fraction, subscript i indicates the air and liquid film interface, subscript v indicates steam, T is the absolute temperature, P is the pressure, and subscript 0 indicates the standard state.

2.3 Model correction under high pressure

As pressure and steam concentration increase, the steam mass transfer process intensifies. An enhanced steam condensation rate can increase the lateral disturbance of the high-concentration air layer, leading to enhanced heat and mass transfer. In general, a correction factor θ [9] is used to represent additional heat transfer. θ is defined based on Eqs. (11)–(13).

$$B = \frac{\omega_{vi} - \omega_{v\infty}}{1 - \omega_{vi}} \tag{11}$$

$$\theta_B = \frac{\ln(1 + B)}{B} \tag{12}$$

$$\theta = 2.98 + 52000 \times \left(7 \times 10^{-5}\right)^{\theta_B} \tag{13}$$

where ω_{vi} is the steam mass fraction near the wall and $\omega_{v\infty}$ is the mainstream steam mass fraction.

2.4 Model validation

Simulations of the COPAIN experiments [33] were performed to determine the accuracy of the condensation model. The geometric model and dimensions of the simulation are shown in Fig. 1.

The dimensions for the experimental setup were 0.5 m long, 0.6 m wide, and 2.0 m high, and one of the sidewalls of the cuboid served as the condensing wall surface. Owing
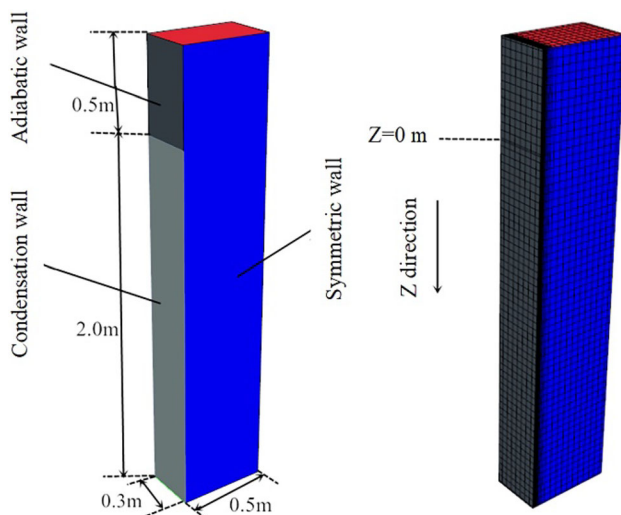
Fig. 1 Geometrical and mesh conditions for the COPAIN experiment

to the better symmetry of the device, only half of the device was calculated to reduce the number of grids and increase the speed of the calculations. The upper part of the device was the velocity inlet, the lower part was the pressure outlet, and the right side was the symmetric wall. The condensation wall was set at a constant temperature and the rest of the wall was set as adiabatic walls. From top to bottom, the mixture flowed in the Z-axis direction, and the junction between the condensing wall and insulation wall was zero. The simulated conditions are listed in Table 1.

Three experimental conditions listed in Table 1 were simulated. The local heat flux along the Z-axis was compared with the experimental values, and the results are shown in Fig. 2.

Figure 2 demonstrates that the variation in the local heat flux along the z-axis matches well with the experimental values. A comparison of the experimental and simulated values at the experimental measurement locations revealed that 91% of the software simulations deviated from the experimental values by less than 10%. The selected model can correctly simulate the heat transfer characteristics of the condensation of steam-containing air under subsequent calculation operating conditions.
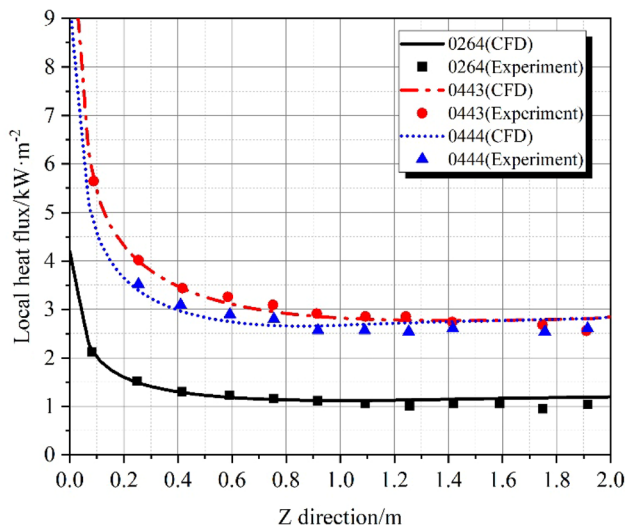
3 Geometrical and mesh conditions

3.1 Geometrical conditions

To examine the heat transfer properties of the heat transfer tubes with an enhanced structure, calculation of heat transfer coefficient for the plain tube is required for comparison. The geometry and mesh model set up in the simulation are shown in Fig. 3. A plain tube with a diameter of 0.038 m and length of 1 m was simulated. The tube was then placed in a cylinder with a radius of 0.3 m. The top and bottom surfaces of the model were set as the velocity inlet and the pressure outlet, respectively. The tube surfaces were set as constant-temperature walls on the condensation wall. In the mesh generating process, the "polyhedral mesh" model was employed. The remainder of the enhanced heat transfer tube was established in a manner similar to that of the plain tube. Only the plain tube was replaced with an enhanced heat transfer tube. Other enhanced heat transfer tube configurations are described later.

The established conditions were similar to those of the 0443 condition of the COPAIN experiment. The pressure was 0.102 MPa, the mainstream speed was 1 m/s, the mainstream temperature was 352.33 K, the condensation wall temperature was 300 K, and the air mass fraction was 0.772.

Table 1 Test conditions for the COPAIN experiment

Test number	Inlet velocity (m/s)	Pressure (MPa)	Inlet temperature (K)	Wall temperature (K)	Air mass fraction
0264	0.52	0.119	344.87	313.28	0.867
0443	1.00	0.102	352.33	300.06	0.772
0444	0.50	0.102	351.53	399.70	0.773

Fig. 2 Model validation results
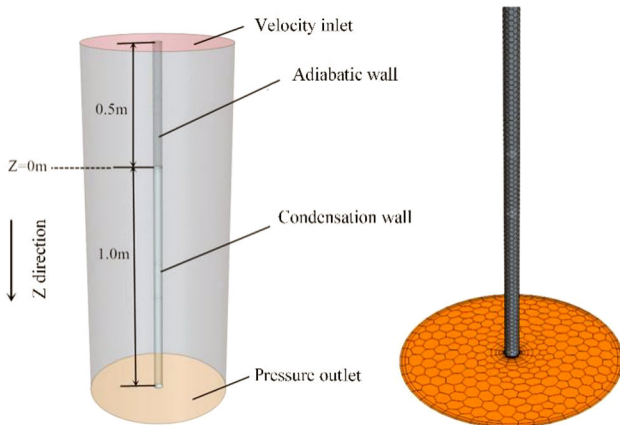
Fig. 3 Geometrical and mesh conditions for the plain tube

3.2 Grid-independent verification

The range of the network size was set as 0.02–0.05 m for the calculation, and the prism layer mesh was adjusted to result in a $Y+$ value less than 1. The calculated results comparing the simulated local heat flux at different network sizes are shown in Fig. 4.

The mesh size had little influence on the heat flux, except a small section of the outlet, which had a deviation of 5% when the mesh size was set to 0.04 m. The rest of
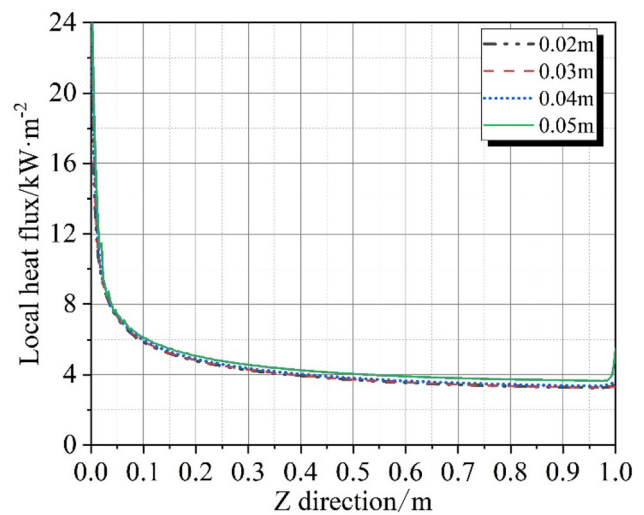
Fig. 4 Grid-independent verification results

the deviation was within 3%. When the grid size was 0.05 m, the calculation results were approximately 10% of the deviation compared to the result of 0.02 m. A grid with a basic size of 0.04 m was initially employed, and the grid convergence index (GCI) [34] proposed by Roache was used to verify the heat flux Φ, where GCI is defined as

$$\text{GCI} = \frac{1.2}{r^a - 1} \left| 1 - \frac{n_c}{n_f} \right| \times 100\% \tag{14}$$

where r is the ratio of the base size of the grid, n is the physical quantity used for verification, subscript c is the coarse grid, and subscript f is the fine grid. a selected according to the discrete format set during CFD calculation, the simulation uses a second-order format that should be selected as 2.

As the GCI is equal to 0.303% and a value less than 5% satisfies the requirement, the base grid size used for subsequent calculations was 0.04 m. Thereafter, the grid independence of the enhanced heat-transfer tube was verified. Of note, the 0.04 m base grid size can be used for other structures.

3.3 Timestep sensitivity verification

The time step was set from 0.005 to 0.4 s for the calculation. The total calculation time was 30 s. The

calculated results of the comparison of the simulated local heat flux at different time steps are shown in Fig. 5. The time step was found to have little effect on the calculation. Thus, a time step of 0.02 s was selected for the calculation; this selection ensures the accuracy of the calculation results.

4 Condensation heat transfer analysis

4.1 Performance of the plain tube

After the steam condenses, the air remains near the wall, forming a concentrated layer of air near the wall. The air mass fraction near the wall is more than 25% greater than that near the mainstream zone. Steam must pass through the air layer to reach the wall for condensation. As the high-concentration air layer increased the steam diffusion resistance, the corresponding condensation heat transfer resistance also increased. Evidently, the high-concentration air layer is an important factor in the heat-transfer process and can be described by the air concentration boundary layer.

$$\frac{\omega_i - \omega_b}{\omega_i - \omega_{main}} = 99\% \tag{15}$$

where ω_i is the air mass fraction at the interface, ω_b is the air mass fraction at the air boundary layer thickness, and ω_{main} is the air mass fraction at the mainstream.

The air boundary layer distribution and its effects on condensation heat flux are shown in Fig. 6, which indicates that the air boundary layer above the tube is thinner and the local heat flux is higher, whereas the air boundary layer below becomes thicker and the local heat flux decreases.
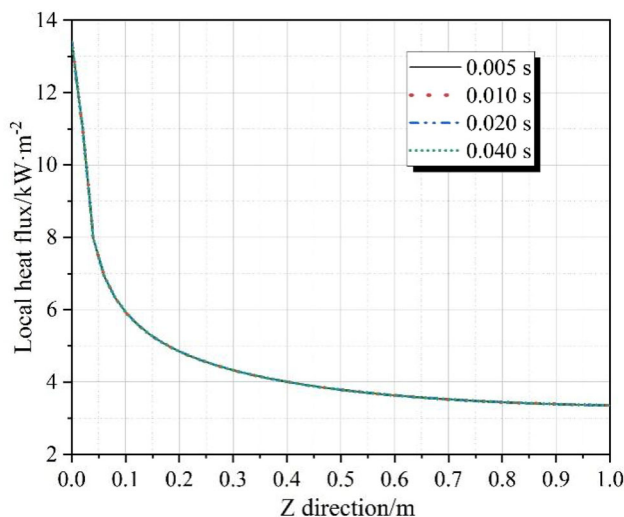

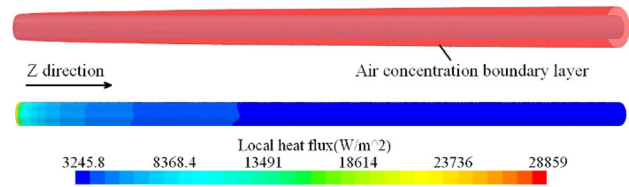**Fig. 5** Timestep sensitivity verification results

Fig. 6 Air concentration boundary layer and local heat flux distribution

The boundary layer thickness versus the local heat flux, radial air mass fraction, density, and fluid velocity distribution are shown in Fig. 7. The shaded portion in the figure represents the plain-tube position.

Figure 7 shows that an air layer formed near the wall, which increased the density of the gas at the wall. As the density of air is greater than that of vapor, owing to the influence of gravity, the velocity of the gas mixture near the wall is greater than that of the mainstream. The air layer flowed downward, resulting in its accumulation and thickening. As the resistance of steam diffusion to the condensation wall increased, the local heat flux along the Z-axis direction gradually decreased, and the change in the air layer thickness was basically the same.

The trends for the air mass fraction and other parameters at different mainstream parameters were the same as those in Fig. 7. The air mass fraction and other parameters were less different from the mainstream parameters at 1–2 cm from the wall. The distance was smaller when the mainstream air mass fraction was small. Further, the distance varied less at different pressures for the same mainstream air mass fraction. A structure of approximately 1–2 cm was required to disturb the air layer. The calculated average condensation heat transfer coefficient of the plain tube was 81.02 W m^{-2} K^{-1}. This value was regarded as the reference value for the enhanced heat-transfer tube.

4.2 Performance of the corrugated tube

The diameter of the corrugated tube trough is 0.038 m, the diameter at the peak is 0.048 m, and the pitch is 0.03 m. The corrugated tube has a potentially disturbing effect inside and outside the tube, a large extended surface, and can withstand high pressures. This tube is generally applied in the power, chemical, and other fields. In this study, the feasibility of this for enhancing steam–air condensation was further evaluated. The boundary condition settings were consistent with those of the plain tube. The heat transfer coefficient of the corrugated tube under this condition was 106.42 W m^{-2} K^{-1}, which was 31.3% higher than that of the plain tube.

The local velocity and heat flux distributions of the corrugated tube are shown in Fig. 8. The arrow points in
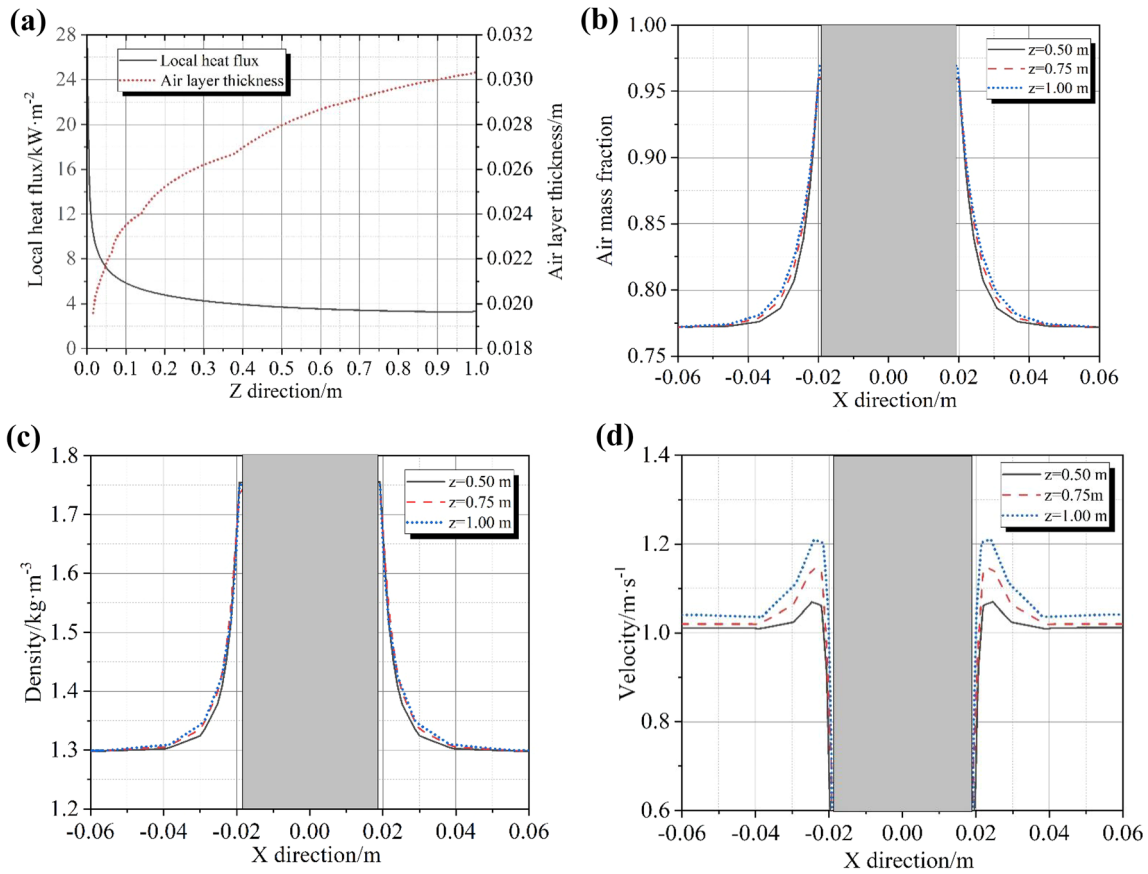
Fig. 7 Plain tube calculation results. **a** Air concentration boundary layer thickness and local heat flux distribution. **b** Radial-air mass fraction distribution. **c** Radial density distribution. **d** Radial velocity distribution
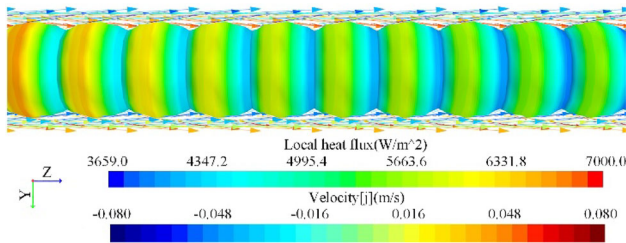
**Fig. 8** Local velocity and local heat flux distribution

the direction of the gas flow, and the arrow represents the velocity in the Y-direction (i.e., the transverse velocity). The corrugated tube had a large heat transfer in the upper part of each peak, and some suppression occurred in the lower part and trough; this result was due to the disturbance caused by the unevenness of the tube when the fluid reached the upper part of the wave crest. The fluid moves outward along the tube with a certain lateral velocity, thinning the air layer and creating a reinforced region in the upper half of the tube. In the upper half of the curved section, the gas flows outward with a greater velocity. The upper and lower sections are too close together to enable sufficient temperature difference for the outward fluid to

flow inward. In fact, there is very little inward flow along the lower section, making the disturbance smaller. At the trough, the air layer has a greater resistance to flow than the plain tube, which can cause a build-up of air at the trough, creating a region of weakened heat transfer.

The heat-transfer region of the corrugated tube was approximately 20% larger than that of the plain tube. In addition, the heat transfer in the reinforced region was significantly greater than that in the same position as the plain tube, enabling the corrugated tube to have a 31% higher heat transfer enhancement than the plain tube.

4.3 Performance of the spiral fin tubes

The spiral fin tube model was based on a plain tube model with a spiral fin piece added. The geometric model is illustrated in Fig. 9.
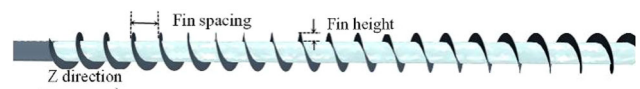

Fig. 9 Geometrical model of the spiral fin tube

The remaining size settings were consistent with the plain tube model, and the selected conditions were the same as those of the plain tube. The fin thickness was set to 0.5 cm and the fin height was set to 1.5 cm. Further, the fins were set to be adiabatic, and the thermal conductivity of the fins was ignored. The heat transfer was only enhanced by perturbing the air boundary layer, resulting in a more conservative result.

The fin spacing was adjusted to 5, 10, 15, and 30 cm. The predicted heat-transfer coefficients are listed in Table 2. The heat transfer coefficient was 92.82 W m^{-2} K^{-1} when the pitch was 5 cm, which was 14.6% stronger than that of the plain tube. Pitches of 5 cm and 30 cm were used for the comparative analysis.

The velocity field and heat-flux distributions at different pitches are shown in Fig. 10. As depicted in the diagram, after the addition of the spiral fins, a portion of the outer fluid flows inward with a transverse velocity under the influence of the temperature difference. Notably, the gas reaching the near-wall surface flows in a spiral direction along the fins, and the fluid that arrives at the top of the fins will block upward flow, causing some disturbance for the gas above the fins. This region forms the reinforced region.

The heat transfer in this region was markedly enhanced. Further, the air below the fins was less disturbed and tended to accumulate. Accordingly, this region formed a weakened region. Increased heat transfer in reinforced area is greater than decreased in weakened area, causing some overall enhancement of the heat transfer. When the pitch of the screw is larger, the bending angle of the fins is smaller, which causes less disturbance to the gas. The vast majority of the gas flows along the fins, with very little gas flowing upward owing to the fins, leading to the formation of a smaller reinforced region above the fins. When the pitch was small, the fins were flat, and most of the gas that reached the fins was blocked by fins and flowed upward, leading to a larger reinforced region, and an enhancement that is approximately 10% higher with a pitch of 5 cm than with a pitch of 30 cm.
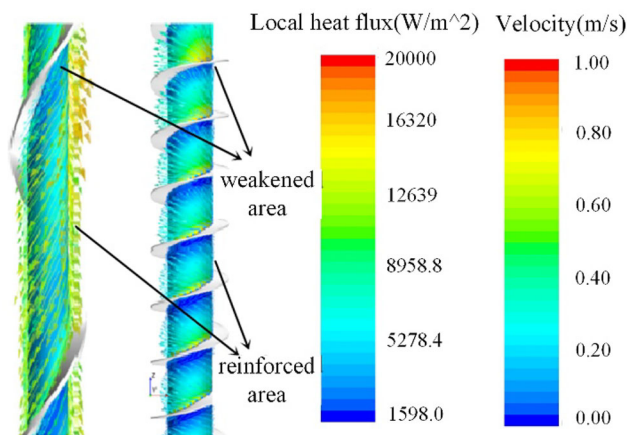
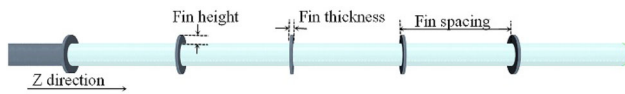**Fig. 10** Local velocity field distribution with a pitch of 30 cm and 5 cm

4.4 Performance of the ring fin tubes

The ring fin tubes are based on the plain tube model with additional fins on the condensing wall, the structure of which is illustrated in Fig. 11. The fin thickness was set to 0.5 cm, and the fin section was set to a constant wall temperature and insulation. The rest of the parameter size, initial conditions, and grid division were consistent with those of the plain tube. The local heat transfer coefficients under the constant wall temperature condition and insulation wall condition at a fin height of 1.5 cm and spacing of 20 cm, are shown in Fig. 12. The shaded part represents the fin position.
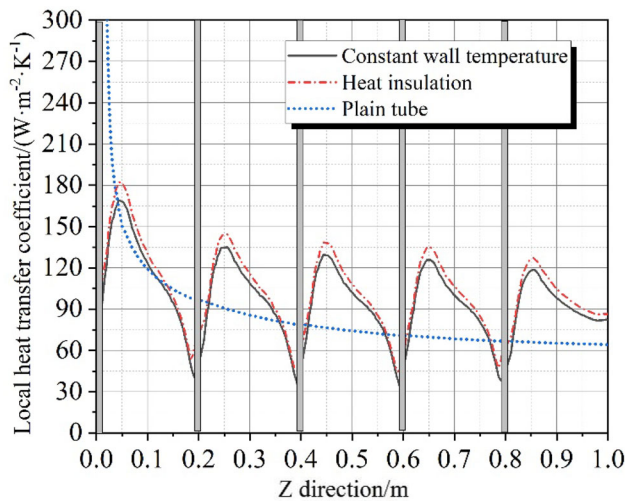
According to Fig. 12, the local heat transfer coefficient at the tube wall exhibits the same trend when the fin is constant and adiabatic. The actual local heat transfer coefficients should be between the constant fin temperature and adiabatic, and because they are relatively close, the temperature on the fin has a negligible effect on the heat flux at the tube wall. Herein, the results were more conservative as the fins were insulated. The average condensing heat transfer coefficient when the fins were adiabatic was 96.65 W m^{-2} K^{-1}. The total heat transfer

Table 2 Comparison of the heat transfer coefficient under different pitches

Fin spacing (cm)	Heat transfer coefficient (W·m^{-2}·K^{-1})	Heat transfer coefficient of plain tube (W·m^{-2}·K^{-1})	Heat transfer enhancement effect
5	92.81	81.02	14.55%
10	89.84	81.02	10.89%
15	89.78	81.02	10.81%
20	89.22	81.02	10.12%
25	87.94	81.02	8.54%
30	84.42	81.02	4.20%

Fig. 11 Geometrical model of the ring fin tube

Fig. 12 Distribution of the local condensation heat transfer coefficient of the ring fin tube

(a)

(b)

Fig. 13 Air concentration boundary layer and local velocity field distribution. **a** Air concentration boundary layer and local heat flux distribution. **b** Local velocity field distribution of the ring fin tube

coefficient can be significantly improved by the disturbance of the fins alone, without the heat transfer coefficient of the fins. The condensing heat transfer coefficient under the selected conditions was 19.3% higher than that of the plain tube.

As shown in Fig. 12, the heat transfer coefficient began to decrease after a rapid increase below the fin and decreased sharply to a minimum in the section above the fin. Figure 13 shows the air boundary layer and local heat flux of the ring fin tube. The velocity vector field ranged from 0.2 to 0.4 m.

Evidently, after being influenced by the fins, a reflux region was formed below the fins, which promotes perturbation of the boundary layer with the mainstream gas owing to upwelling, ultimately producing a peak in heat flux below the fins. Most of the gas flows outward when the fluid flows upward to the fins, forming a stagnant zone below the fins, where the flow velocity is low and the air layer builds up, resulting in less heat transfer over the distance below the fins.

Below the vortex generated by the reflux, the fluid began to flow normally downward, and the trend of the heat flux change was basically the same as that of the initial section of the plain tube. The fluid continued to flow downward, and upon arrival at the top surface of the fins, it was blocked by the fins, with most of the gas flowing outward along the fins. A large retention zone was also formed in the section above the fins, where the flow velocities were low, and a high-concentration air layer was generated. As

the heat flux in the reflux region is significantly higher than that in the plain tube, only a small part of the heat flux above the fins is lower than that in the plain tube, which significantly improves the overall heat transfer coefficient under the selected conditions compared to the plain tube. The ring-fin tube has a better heat-transfer strengthening effect.

4.4.1 Effect of fin height on heat transfer

To evaluate the effect of fin height on heat transfer, the fin height was calculated by adjusting the fin height at intervals of 0.5 cm from 0.5 to 4 cm, while keeping the fin thickness and fin spacing constant. A comparison of the heat transfer coefficient under different fin heights is shown in Table 3. The local heat transfer coefficients are shown in Fig. 14, and the velocity field distributions at fin heights of 1, 1.5, and 4 cm are shown in Fig. 15.

The coefficient of heat transfer was greatest at a fin height of 1.5 cm and gradually decreased as the fin height increased. The calculation of the plain tube revealed an air layer thickness of approximately 1–2 cm. Notably, the best results were obtained when the fin height was 1.5 cm. A fin height less than 1.5 cm had less effect on the air layer disturbance and the enhanced heat transfer. Based on Fig. 14, at a fin height of 1.5 cm, the peak of the local heat transfer coefficient below the fin was the largest. As the fin height increased, the peak gradually moved backward and decreased, and the average heat transfer coefficient gradually decreased.

From the local velocity field, there is a certain disturbance to the gas at a fin height of 1 cm, which causes reflux under the fin. The heat transfer in the reflux region was larger, but the reflux region was smaller than the fin height of 1.5 cm. When the fin height was 4 cm, owing to the relatively large fin height, most of the fluid flowing from the outside to the wall did not reach the wall, only near the edge of the fins to form a reflux region. Further, the air near the wall was less disturbed. Below the reflux region, the gas mixture was influenced by the reflux region, and the lower fins had a certain radial velocity, resulting in peaks below the reflux region, which were smaller at higher fin heights owing to less radial perturbation. The best enhancement was 20.2% at a fin height of 1.5 cm. A fin height of 1.5 cm was employed in subsequent studies.
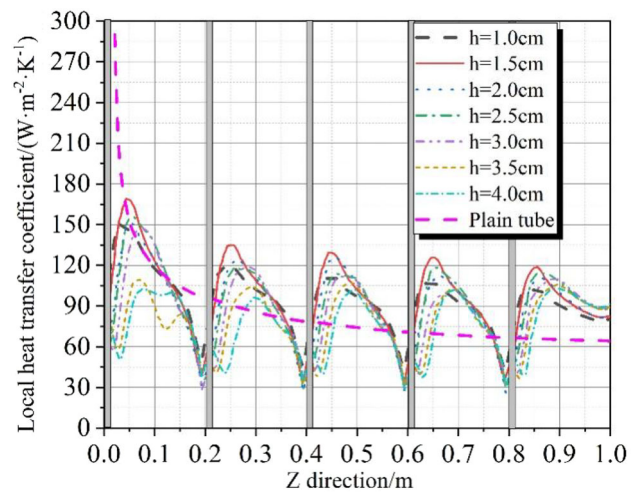

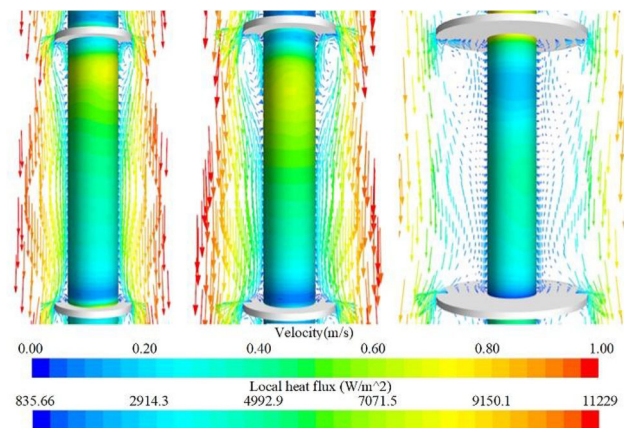**Fig. 14** Distribution of the local heat transfer coefficient under different fin heights

Fig. 15 Local velocity field under different fin heights

4.4.2 Effect of fin spacing on heat transfer

Although the other settings were unchanged, the fin spacing was adjusted to 10, 20, and 30 cm. The local heat-

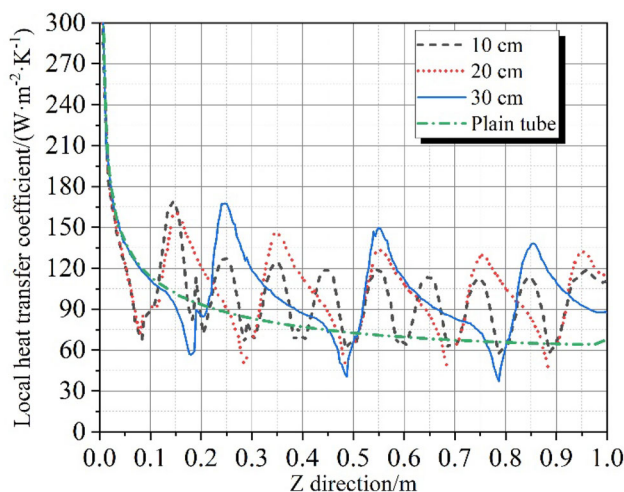**Table 3** Comparison of the heat transfer coefficient under different fin heights

Fin height (cm)	Heat transfer coefficient (W·m^{-2}·K^{-1})	Heat transfer coefficient of plain tube (W·m^{-2}·K^{-1})	Heat transfer enhancement effect
0.5	91.34	81.02	12.73%
1.0	94.35	81.02	16.45%
1.5	96.65	81.02	19.29%
2.0	93.29	81.02	15.14%
2.5	89.42	81.02	10.36%
3.0	85.75	81.02	5.83%
3.5	82.47	81.02	1.79%
4.0	80.12	81.02	-1.11%

transfer coefficients for different fin spacings are shown in Fig. 16. The calculated average heat transfer coefficients were 89.13, 96.65, and 95.16 W m^{-2} K^{-1}, respectively. When the fin spacing was small (e.g., 10 cm), the return region generated below the fins was influenced by the next fin, and the upward flow was reduced, thereby reducing the perturbation of the return region. The peak below the fins was smaller when the fin spacing was 10 cm, and the average heat-transfer coefficient decreased significantly. When the distance between the fins was large, the reflux regions under the fins were almost the same. The trend of the reflux region under the fins was almost the same as the downward trend of the inlet section of the plain tube, and the size of the region above each fin that reduces the heat transfer was almost the same. The number of fins with a spacing of 20 cm was greater than that with a spacing of 30 cm. If the enhancement of heat transfer of the fins was considered, a better enhancement of heat transfer occurred with a fin spacing of 20 cm.

4.5 Analysis of heat transfer enhancement under different working conditions

4.5.1 Comprehensive analysis of heat transfer enhancement at different air mass fractions

Each tube was analyzed to assess the heat transfer enhancement at different air mass fractions. The selected pressure was atmospheric pressure, the wall subcooling degree was 52.33 K (unchanged), and the air mass fractions were adjusted to 0.1, 0.2, 0.3, …, 0.9 for each reinforced structure calculation. After the calculations were performed, the condensed heat transfer coefficients of various structures at different air mass fractions were calculated and compared. The predicted results are shown in Fig. 17.

The trend is essentially the same for different structures, with decreasing heat transfer coefficients as the air mass fraction increases. The smaller the air mass fraction, the greater the decrease in the heat transfer coefficient; this is due to an increase in the air mass fraction in the wall during the formation of the air layer concentration. The boundary layer thickness increases the resistance to steam through the air layer, causing continuous decline of the heat transfer.

At atmospheric pressure, the best enhancement of heat transfer among the simulated structures was achieved by the ring fin tubes, with enhanced heat transfer of approximately 22–24% for every air mass fraction. The enhancement in the heat transfer of the corrugated tube was lower than that of the ring fin tubes when the air mass fraction was less than 0.6. The corrugated tube exhibited a favorable heat transfer enhancement when the air mass fraction was high. The best enhancement in the heat transfer reached 27.4% when the air mass fraction was 0.9. At atmospheric pressure, spiral fin tubes for strengthening the effect were poor. Further, when the air mass fraction was less than 0.5, the enhancement of heat transfer was similar to that of a plain tube. The enhancement of the heat transfer was lower than that of the plain tube when the air mass fraction was less than 0.3. When the air mass fraction was high, a certain enhancement in heat transfer occurs, and the value is approximately 10%. The best enhancement in heat transfer was 14.0% when the air mass fraction was 0.9.

Spiral fin tubes exhibit different enhancements in heat transfer under different air mass fractions owing to the large influence of the air mass fraction on the weakened region. When the mainstream air mass fraction was 0.8, the

Fig. 16 Comparison of the local heat transfer coefficients with different fin spacing
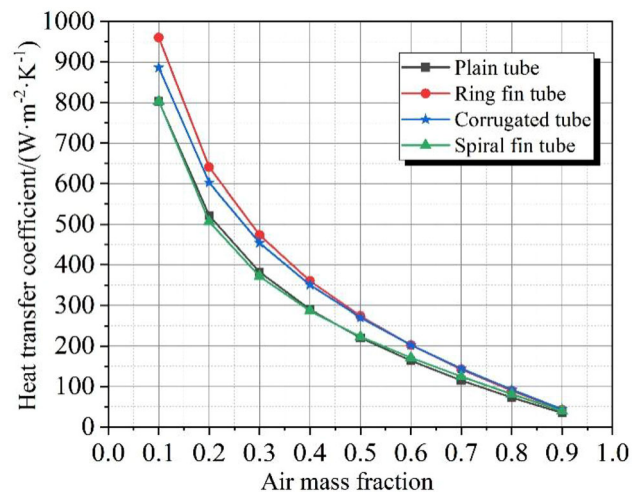
Fig. 17 Comparison of the heat transfer coefficients under different air mass fractions

maximum air mass fraction below the plain tube was 0.972, and the maximum air mass fraction below the spiral fin tube fins was 0.976 in the weakened section owing to the air buildup. Although the air mass fraction was greater than that of the plain tube, the larger amount was less, and the heat transfer enhancement of the region above the fins was markedly greater than that of the plain tube at the same location, somewhat reinforcing the spiral fin tube at a high air mass fraction. When the mainstream air mass fraction was 0.2, the maximum air mass fraction of the plain tube was 0.932 and the maximum air mass fraction of the weak region of the spiral fin tube was 0.966. The weakened region had a large weakening effect, and the enhancement of the heat transfer was close to or insufficient to counteract the effect of the weakened region. The enhancement in the heat transfer of the spiral fin tube was approximately 3% less than that of the plain tube when the mainstream air mass fraction was low.

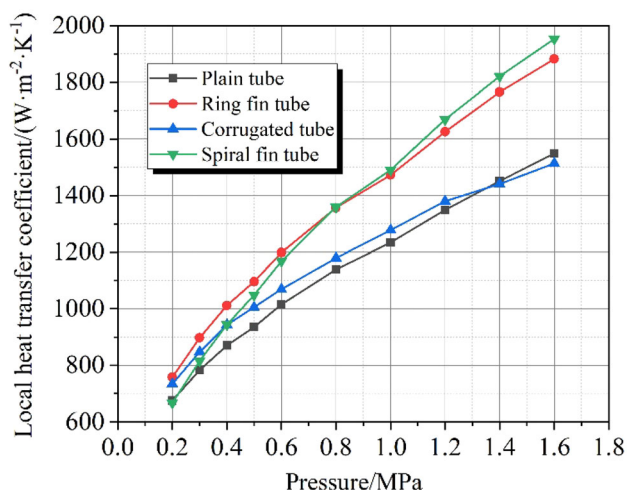### 4.5.2 Comprehensive analysis of heat transfer enhancement at different pressures

Each tube was analyzed to evaluate the heat transfer enhancement at different pressures. By keeping the air mass fraction of 0.4 and the wall subcooling degree of 50 °C constant, the pressure interval of 0.1 MPa was set from 0.2 to 0.6 MPa, and the interval of 0.2 MPa was set from 0.6 to 1.6 MPa. The above structures were calculated separately. The calculated condensation heat transfer coefficients are shown in Fig. 18.

As the gas pressure increased, the heat transfer coefficients of the different structures gradually increased; this is because as the pressure increased, the saturation temperature of the steam increased, and the molecular thermal

motion of the molecules became stronger, assisting the steam with its efforts to reach the wall for condensation, which enhances the heat transfer.

As the pressure increased, the heat transfer enhancement of the ring fins gradually increased from 12.2 to 21.7%. The enhancement in the heat transfer of the corrugated tube was 8.6% at a pressure of 0.2 MPa. The enhanced effect decreased as the pressure increased, and the enhancement of heat transfer was worse than that of the plain tube when the pressure was more than 1.4 MPa; this is because, as the pressure increases, the enhancement of the heat transfer of the plain tube significantly increases. The corrugated tube has less disturbance, making the lower section of the reinforced region of the enhancement of heat transfer more similar to that of the plain tube. The trough at the air layer has a greater accumulation, and because of the increased molecular thermal motion, the trough below the original strengthening of the region has more air, weakening the heat transfer of the region, leading to poor heat transfer at higher pressures.

The spiral fin tube had reduced heat transfer at low pressures. At a pressure of 0.2 MPa, the heat transfer coefficient was worse than that of the plain tube. As pressure increased, the enhancement of heat transfer began to increase at a pressure of 1.6 MPa, with an enhancement of approximately 26.1%. This result is because gas temperature is lower at lower pressures, less molecular thermal motion occurs, and the thick air layer near the wall moves along the fin spiral angle. The fluid blocked by the fins had a smaller upward velocity and a smaller region of upward disturbance, resulting in reduced heat transfer at lower pressures. When the pressure was higher, the saturation temperature was higher, and the molecular thermal movement of molecules was accelerated. Owing to fin blocking, the upward velocity is greater, and the disturbance to the air is noticeable and extensive. On the back half of the tube, the maximum air mass fraction in the weakened region below the fins differs less from that in the plain tube. The heat transfer in the weakened region was less different from that in the plain tube at the same location, causing the spiral fin tubes to exhibit a very good enhancement in heat transfer under high pressure.

5 Conclusion

To enhance the steam–air condensation heat transfer, numerical analyses were performed on plain, corrugated, and fin tubes. The simulation results for the plain tube revealed that the key factor affecting condensation heat transfer is the high-concentration air layer near the wall surface. To effectively disturb the air boundary layer, corrugated, spiral fin, and ring fin tubes were designed and

Fig. 18 Comparison of the heat transfer coefficient under different pressures

numerically analyzed. A wide range of simulations was performed on various tubes under different air mass fractions and pressures, and the applicability of different structures under different conditions was obtained. The main conclusions are as follows:

1. When steam condenses, an air layer forms near the tube. The high-concentration air layer is the key factor affecting heat transfer. The thickness of the high-concentration air layer was found to be greater than 2 cm. To enhance the condensation heat transfer, additional structures should be designed to disturb the air layer and promote the gas mixture between the near-wall and mainstream regions. The structure that facilitates the accumulation of the air layer reduces the condensation heat transfer within a certain range of parameters.

2. The corrugated tube has a large extended surface that can disturb the air layer. This tube exhibited a better enhancement of the heat transfer at atmospheric pressure. In fact, the maximum enhancement was 27.4% higher than that of a plain tube. Under violent molecular thermal motion, the disturbance effect of the corrugated tube was too small to play a role. Therefore, the enhancement of the corrugated tube under higher pressure is poor. The enhancement of the corrugated tube was below 10%. When the pressure was higher than 1.4 MPa, the heat transfer coefficient was lower than that of the plain tube.

3. Air tends to accumulate under the fins of spiral fin tubes and this region forms a weakened region. The gas above the fins experiences an effective disturbance and this region forms the reinforced region. When the fin spacing was large, the disturbance effect worsened. At atmospheric pressure, the weakened regions had a greater effect on heat transfer. The enhancement in the heat transfer of the spiral fin tube at atmospheric pressure was poor, with a maximum enhancement of only 14%. When the air mass fraction was less than 0.4, the heat-transfer coefficient was approximately 2% lower than that of the plain tube. Owing to the strong molecular thermal motion, fins have a greater disturbance to the air. The reinforced region at high pressure has a greater effect on the heat transfer. The enhancement of the spiral fin tube was better under high pressure, with a maximum enhancement of 26.1%.

4. When the rib height was 1.5 cm and fin spacing was 20 cm, the ring fin tube exhibited a good disturbance of the air layer. A large region of air was disturbed below the fins, and a smaller region of air tended to accumulate. The ring fin tube enhanced the heat transfer under all calculated working conditions and could adapt to changing situations in the event of accidents. At all air mass fractions, the ring fin tube had a good disturbance effect on the air, with an enhancement of approximately 20% in all cases, and a maximum enhancement of 24.2%. The ring fin tube also exhibited a certain enhancement in heat transfer at different pressures. The minimum and maximum enhancements were 12.2% and 21.7%, respectively.

References

1. S. Sheykhi, S. Talebi, M. Soroush et al., Thermal-hydraulic and stress analysis of AP1000 reactor containment during LOCA in dry cooling mode. Nucl. Sci. Technol. **28**, 73 (2017). https://doi.org/10.1007/s41365-017-0233-8

2. Y. Cheng, M. Zheng, Y. Wang et al., Study on the long-term passive cooling extension of AP1000 reactor. Nucl. Sci. Technol. **24**, 040601 (2013). https://doi.org/10.13538/j.1001-8042/nst.2013.04.013

3. J. Rosa, A. Escrivá, L. Herranz et al., Review on condensation on the containment structures. Prog. Nucl. Energy **51**(1), 32–66 (2009). https://doi.org/10.1016/j.pnucene.2008.01.003

4. X. Han, M. Zheng, Y. Yang, Concept research on general passive system. Nucl. Power. Eng. **30**(03), 115–118 (2009). (**(in Chinese)**)

5. S. Sheykhi, S. Talebi, Analysis of maximum pressure in VVER1000/V446 reactor containment for LOCA and MSLB. Nucl. Sci. Technol. **28**, 132 (2017). https://doi.org/10.1007/s41365-017-0288-6

6. G. Tang, H. Hu, D. Niu et al., Advances in vapor drop wise condensation heat transfer. Chin. Sci. Bull. **65**(17), 1653–1676 (2020). https://doi.org/10.1360/TB-2019-0577

7. L. Wu, H.J. Jia, X. Ma et al., Research on the effect of Reynolds correlation in natural convection film condensation. Nucl. Sci. Technol. **28**, 85 (2017). https://doi.org/10.1007/s41365-017-0240-9

8. C. Chantana, S. Kumar, Experimental and theoretical investigation of air-steam condensation in a vertical tube at low inlet steam fractions. Appl. Therm. Eng. **54**(2), 399–412 (2013). https://doi.org/10.1016/j.applthermaleng.2013.02.024

9. H. Bian, Z. Sun, M. Ding et al., Local phenomena analysis of steam condensation in the presence of air. Prog. Nucl. Energy. **101**, 188–198 (2017). https://doi.org/10.1016/j.pnucene.2017.08.002

10. M. Joseph, G. Mathew, G. Krishnaraj et al., Numerical simulation of liquid-gas interface formation in long superhydrophobic microchannels with transverse ribs and grooves. Exp. Comput. Multiph. Flow **2**(3), 162–173 (2020). https://doi.org/10.1007/s42757-022-0132-z

11. M. Murase, Y. Kataoka, T. Fujii, Evaporation and condensation heat transfer with a noncondensable gas present. Nucl. Eng. Des. **141**(1–2), 135–143 (1993). https://doi.org/10.1016/0029-5493(93)90098-T

12. D. Othmer, The condensation of steam. Ind. Eng. Chem. **21**, 577–583 (1929)

13. S. Park, M. Kim, K. Yoo, Condensation of pure steam and steam-air mixture with surface waves of condensate film on a vertical wall. Int. J. Multiph. Flow. **22**(5), 893–908 (1996). https://doi.org/10.1016/0301-9322(96)00020-1

14. H. Al-Diwany, J. Rose, Free convection film condensation of steam in the presence of non-condensing gases. Int. J. Heat Mass Transf. **16**(7), 1359–1369 (1973). https://doi.org/10.1016/0017-9310(73)90144-0

15. H. Uchida, A. Oyama, Y. Togo, Evaluation of post-incident cooling systems of light-water power reactors, in *Third International Conference on the Peaceful Uses of Atomic Energy* (1965), pp. 93–104

16. S. Zhou, Y. Li, Y. Sun et al., Evaluations and classifications of the bundle effects on steam condensation based on broad pressure range experiments. Prog. Nucl. Energy **135**, 103695 (2021). https://doi.org/10.1016/j.pnucene.2021.103695

17. J. Su, Z. Sun, G. Fan et al., Experimental study of the effect of non-condensable gases on steam condensation over a vertical tube external surface. Nucl. Eng. Des. **262**, 201–208 (2013). https://doi.org/10.1016/j.nucengdes.2013.05.002

18. H. Liu, N. Todreas, M. Driscoll, An experimental investigation of a passive cooling unit for nuclear plant containment. Nucl. Eng. Des. **199**(3), 243–255 (2000). https://doi.org/10.1016/S0029-5493(00)00229-6

19. A. Dehbi, A generalized correlation for steam condensation rates in the presence of air under turbulent free convection. Int. J. Heat Mass Transf. **86**, 1–15 (2015). https://doi.org/10.1016/j.ijheatmasstransfer.2015.02.034

20. P. Peterson, Theoretical basis for the Uchida correlation for condensation in reactor containment. Nucl. Eng. Des. **162**, 301–306 (1996). https://doi.org/10.1016/0029-5493(95)01125-0

21. J. Collier, *Convective Boiling and Condensation* (McGraw-Hill, UK, 1972), pp.314–359

22. E. Sparrow, W. Minkowycz, M. Saddy, Forced convection condensation in the presence of noncondensables and interfacial resistance. Int. J. Heat Mass Transf. **10**, 1829–1845 (1967). https://doi.org/10.1016/0017-9310(67)90053-1

23. A. Dyj, C. Jwlb, A. Dk et al., Effective reduction of non-condensable gas effects on condensation heat transfer: surface modification and steam jet injection. Appl. Therm. Eng. **174**, 115264 (2020). https://doi.org/10.1016/j.applthermaleng.2020.115264

24. X. Dong, X. Ma, Y. Zhang et al., Experimental investigation of dropwise condensation in the presence of non-condensable gas. J. Eng. Thermophys. **25**(6), 1001–1003 (2004)

25. G. Fan, P. Tong, Z. Sun et al., Experimental study of pure steam and steam–air condensation over a vertical corrugated tube. Prog. Nucl. Energy **109**, 239–249 (2018). https://doi.org/10.1016/j.pnucene.2018.08.020

26. P. Tong, G. Fan, Z. Sun et al., Experimental study of steam-air condensation over a vertically longitudinal finned tube. Int. J. Heat Mass Transf. **89**, 1230–1238 (2015). https://doi.org/10.1016/j.ijheatmasstransfer.2015.06.036

27. Z. Niu, H. Guo, G. Fan, Study of different surface treatment methods influence on the condensation hear transfer characteristics of vertical tube external surface, in *Progress Report on China Nuclear Science & Technology* (2019), pp:169–175. https://doi.org/10.26914/c.cnkihy.2019.056509

28. P. Peterson, Theoretical basis for the Uchida correlation for condensation in reactor containments. Nucl. Eng. Des. **162**(2–3), 301–306 (1996). https://doi.org/10.1016/0029-5493(95)01125-0

29. E. Sparrow, W. Minkowycz, M. Saddy, Forced convection condensation in the presence of noncondensables and interfacial resistance. Int. J. Heat Mass Transf. **10**(12), 1829–1845 (1967). https://doi.org/10.1016/0017-9310(67)90053-1

30. B. Quan, H. Bian, M. Ding et al., Numerical analysis on the characteristics of steam condensation in presence of air under vertical tube bundle conditions. Nucl. Power Eng. **40**(5), 29–34 (2019). https://doi.org/10.13832/j.jnpe.2019.05.0029

31. J. Rosa, A. Escriva, L. Herranz et al., Review on condensation on the containment structures. Prog. Nucl. Energy **51**(1), 32–66 (2009). https://doi.org/10.1016/j.pnucene.2008.01.003

32. H. Bian, Z. Sun, M. Ding et al., Numerical simulations on steam condensation heat transfer characteristics in the presence of air. J. Harbin Eng. Univ. **40**(2), 426–432 (2019). https://doi.org/10.11990/jheu.201709070 **(in Chinese)**

33. M. Kawakubo, M. Aritomi, H. Kikura, T. Komeno, An experimental study on the cooling characteristics of passive containment cooling systems. J. Nucl. Sci. Technol. **46**(4), 339–345 (2009). https://doi.org/10.1080/18811248.2007.9711539

34. P. Roache, Perspective: a method for uniform reporting of grid refinement studies. J. Fluids Eng. **116**(3), 405–413 (1994). https://doi.org/10.1115/1.2910291